

Riukojietna, a small low-altitude ice cap that may have persisted through the Holocene: Evidence from combining cosmogenic multi-nuclide dating and lacustrine sediment records

Arjen P. Stroeven^{1,2}, Gunhild C. Rosqvist^{1,2}, Allie J. Koester³, Jane L. Andersen^{1,4}, Carl-Anton Wahlström⁵, Nathaniel A. Lifton^{3,6}

¹ Department of Physical Geography, Stockholm University, 106 91 Stockholm, Sweden

² Bolin Centre for Climate Research, Stockholm University, 106 91 Stockholm, Sweden

³ Department of Earth, Atmospheric, and Planetary Sciences, Purdue University, West Lafayette IN 47907 USA

⁴ Research Centre for the Built Environment, Energy, Climate, and Water Technology, VIA University College, 8700 Horsens, Denmark

⁵ IKNI AS, PO Box 6646, 0129 Oslo, Norway

⁶ Purdue Rare Isotope Measurement Laboratory (PRIME Lab), Department of Physics and Astronomy, Purdue University, West Lafayette IN 47907, USA

Correspondence to: Arjen P. Stroeven (arjen.stroeven@natgeo.su.se)

Supplementary Information

Text: S1-S4

Figures S1-S5

S1 Model description

We calculate the total production rate at each sample site (P_{tot} , at $\text{g}^{-1} \text{yr}^{-1}$), under prescribed ice thickness histories for that site, using the LSDn scaling framework (Lifton et al., 2014; Lifton, 2016) and account for the depth-dependence of spallogenic and muogenic production due to ice thickness and erosional histories for one-year time steps over a modeled glacial history since 20 ka. We account for erosion using a Lagrangian framework, which tracks the production changes in the sample as it moves towards the surface over time, including ice-shielding effects (e.g., Knudsen et al., 2019). In practice this involves back-calculating sample depths within the bedrock according to subglacial erosion rate, time step, and model duration, beneath time-dependent ice thicknesses, such that the sample ends up at the ground surface at present. If erosion is zero, only the shielding effects of the ice-thickness history over the ground surface are modeled.

The spallogenic production rate for each nuclide with depth is calculated following the equation:

$$P_{sp_cor,i}(t) = P_{sp,i} * e^{-\left(\frac{\rho_{ice} * z_{ice}(t)}{\Lambda_{sp,ice}} + \frac{\rho_{rock} * z_{rock}(t)}{\Lambda_{sp,rock}}\right)} \quad (1)$$

where $P_{sp,i}$ is the site-specific spallation production rate of nuclide i at the ground surface (at $\text{g}^{-1} \text{yr}^{-1}$), ρ_{ice} is the density of ice (0.92 g cm^{-3}), $z_{ice}(t)$ is the prescribed ice thickness over time (cm), $\Lambda_{sp,ice}$ is the spallation attenuation length for ice at high latitudes (140 g cm^{-2}), $\Lambda_{sp,rock}$ is the spallation attenuation length for rock at high latitudes (150 g cm^{-2}) (Lifton et al., 2014; Marrero et al., 2016; Phillips et al., 2016), ρ_{rock} is rock density (2.65 g cm^{-3}), and $z_{rock}(t)$ is the sample depth within the bedrock over time (cm). We calculate the depth-dependence of muon production for each nuclide over time using Model 1a of Balco (2017). This code accounts for depth-dependent changes in the energy spectrum of the muon flux per the formulations of Heisinger et al. (2002a, b) with resulting effects on nuclide production. We calculate the total production ($P_{tot,i}$) at each depth (time) interval by summing the spallogenic and muogenic production.

The cosmogenic nuclide concentrations of nuclide i are then calculated from 20 ka to present following the equation:

$$N_i = [N_{i,0} * e^{-\lambda_i dt}] + \left[\frac{P_{tot,i}}{\lambda_i} * (1 - e^{-\lambda_i dt}) \right] \quad (2)$$

where N_i is the concentration of nuclide i (at g^{-1}), $N_{i,0}$ is the concentration of nuclide i (at g^{-1}) produced from the previous time step (0 at 20 ka), λ_i is the decay constant of nuclide i , $P_{tot,i}$ is the total production rate at the sample depth for nuclide i (at $\text{g}^{-1} \text{yr}^{-1}$), and dt is the time step of 100 years.

S2 Uncertainty estimates

We estimate uncertainties in the model output by accounting for the production rate uncertainty in each nuclide via a simple Monte Carlo method using 1000 iterations. Since the production rate estimates and their uncertainties are means and standard deviations, we draw a production rate randomly for each iteration from a normal distribution characterized by the calibrated mean and standard deviation. We then run the forward model for 1000 iterations and store the predicted modern nuclide concentrations from each iteration. Finally, we calculated the mean and standard deviation of the predicted modern values for each nuclide and plot the results $\pm 2\sigma$.

S3 Subglacial erosion

Effects of subglacial erosion are incorporated via an optional erosion rate ranging from 0.01 mm yr^{-1} typical of polar glaciers to 0.1 mm yr^{-1} suggested for thin temperate plateau glaciers on crystalline bedrock (Hallet et al., 1996), tied to a specified minimum ice thickness threshold for erosion to occur. However, constraints are lacking on the ice thickness required to reach pressure-melting conditions in this setting, especially for the bedrock knob where higher subglacial pressure on its upstream side

may have resulted in the production of subglacial water which could have facilitated the sliding of ice across the sampling site or refreezing and plucking. Indeed, common and prominent striations were noted in the field at the sampling locations on the knob, suggesting glacial sliding there (Fig. S5). Given the reconstructed ice thickness histories, we evaluated minimum erosional thresholds of 10, 20, and 30 m with respect to the resulting cosmogenic nuclide concentrations and found little difference in predicted concentrations when the threshold is between 10 and 30 m with our modeled scenarios. Since we model our maximum ice thickness over our sample locations during the Holocene as 34 m (mean of 35 and 33 m over Riuko 16-001/2 and Riuko 16-003/4, respectively; Table S4), based on the LIA thickness reconstruction, we set the minimum erosional threshold at 30 m.

S4 Pre-Holocene ice-thickness history

The precise ice-thickness history for the location of our sampling sites since 20 ka is poorly constrained except that it was fully shielded until local deglaciation from the Fennoscandian Ice Sheet (FIS) retreat. The FIS margin was slowly pivoting in this region because the ice margin retreat from the north and particularly from the east wildly outpaced retreat from the west (Stroeve et al., 2016; Ploeg and Stroeve, 2025). Detailed reconstruction of the ice sheet margin using glacial geomorphology and the evolution of ice-dammed lakes in an area immediately east and north of our study area, reveals that the reconstructed margins by Stroeve et al. (2016) for 10.0 and 9.9 ka were overall correct, but showed a lot of detailed crenulations that remain unresolved on an ice sheet-scale (Ploeg and Stroeve, 2025). This lends strength to the outline of the reconstructed ice sheet margins across Riukojietna, only kilometers away from the Ploeg and Stroeve (2025) detailed reconstruction. In the Stroeve et al. (2016) reconstruction, the ice margin would have retreated approximately in a WSW-ENE direction across the catchment. The ice margin was likely steep, as evidenced by the many deep lakes it dammed in the course of its retreat across the landscape. For ice thickness reconstructions, this means that the sampling sites were under deep ice until local FIS deglaciation somewhere around 9.8 ka. In the process of FIS retreat, Riukojietna must have separated from the main margin and become its own entity and here is where thinning potentially starts to become important for subglacial nuclide production. We modeled this broadly by assuming a linear decrease in ice thickness over Riukojietna from 200 m at 20 ka to 50 m by 9.9 ka. Subsequent ice-thickness changes from 9.8 ka through present are described in section 5.3 in the main text.

S5 Supplemental figures

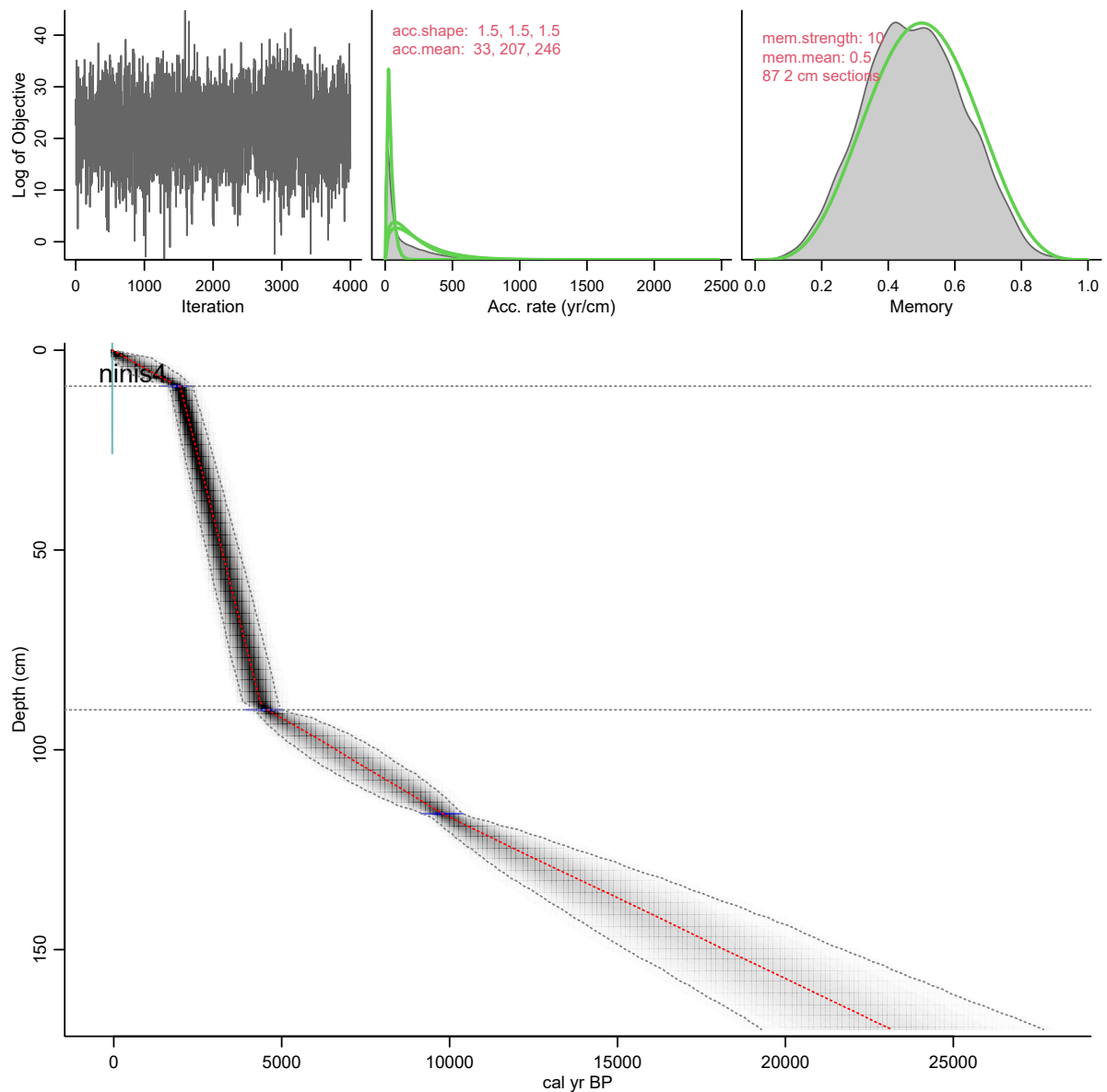


Figure S1: Age-depth model output from the Bayesian accumulation age-modelling software of Blaauw and Christen (2011) for Pajep Luoktejaure (Rbacon 3.5.2) using three radiocarbon tie points (samples Ua-14024, Ua-14025, and Ua-16628; Table 3) and a surface age of -48 BP (1998 CE). In the solution space, the median is shown (red) with the minimum and maximum estimates on either side (95% probability). Extrapolation to the bottom of the core (169 cm depth) is shown, but has no significance.

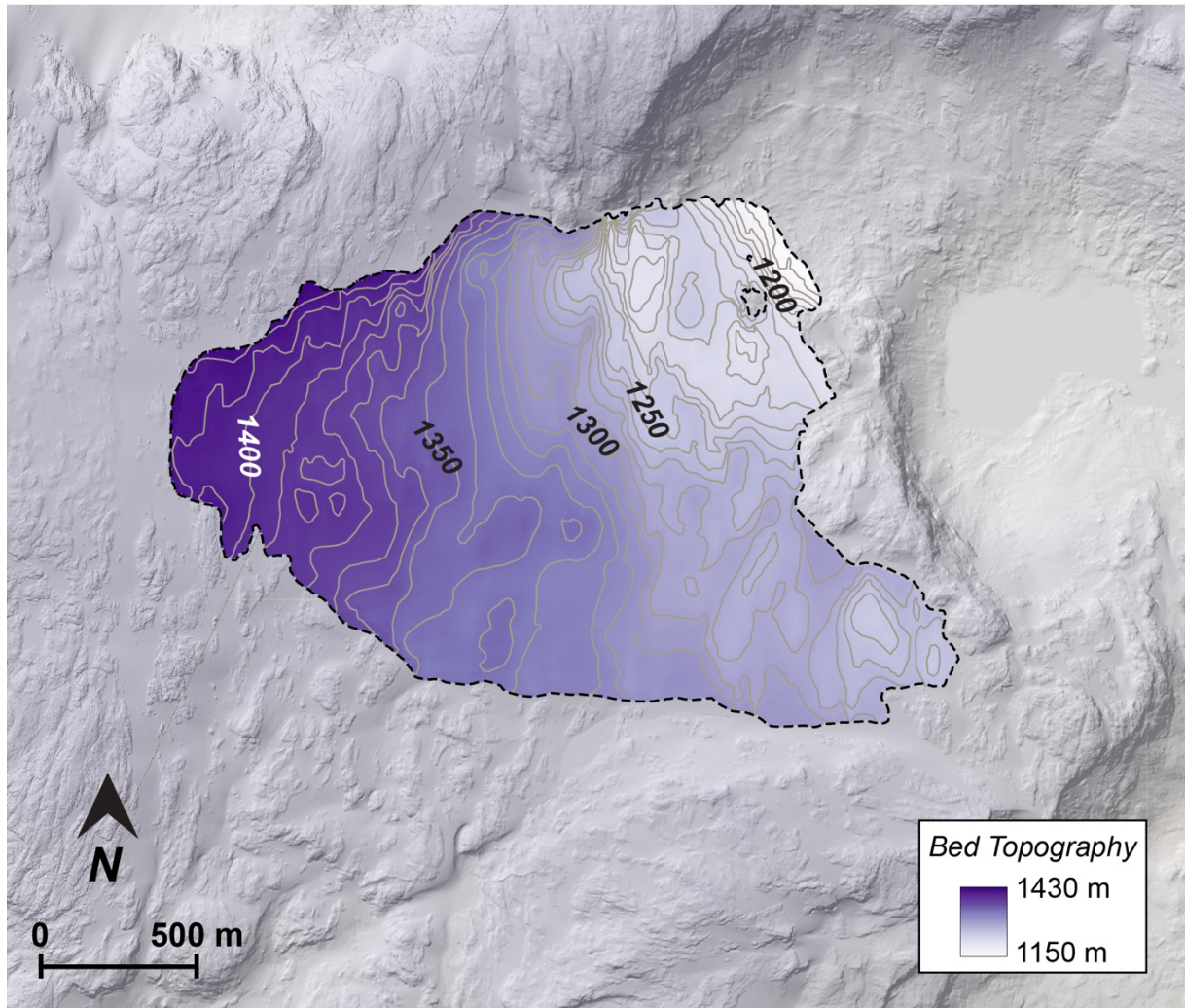


Figure S2: Bed topography constructed from interpolated GPR measurements in 2011, 2012, and 2015. Contour interval 10 m. Surrounding topography is 2 m LiDAR from 2015 provided by © Lantmäteriet (<https://www.lantmateriet.se/>).

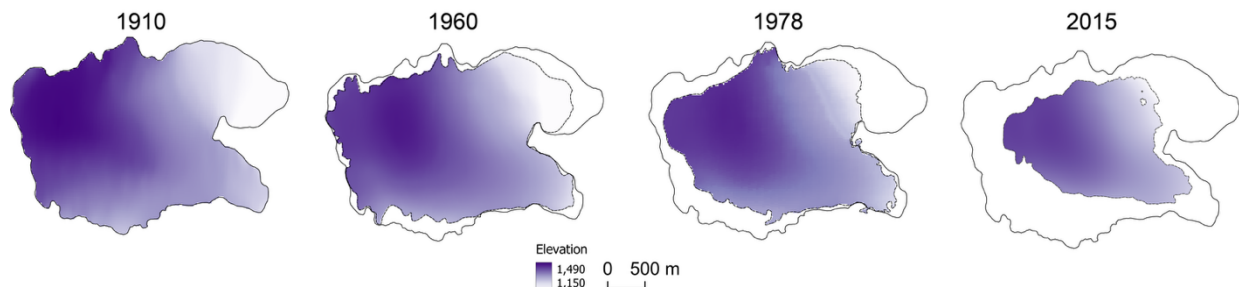


Figure S3: Elevation reconstructions of the Riukojietna ice cap from 1910, 1960, 1978, and 2015 with respect to its maximum extent during the LIA (1910). The 1960 and 1978 elevations have been corrected to better compare to the 2 m LiDAR DEM from 2015 (Fig. S2).

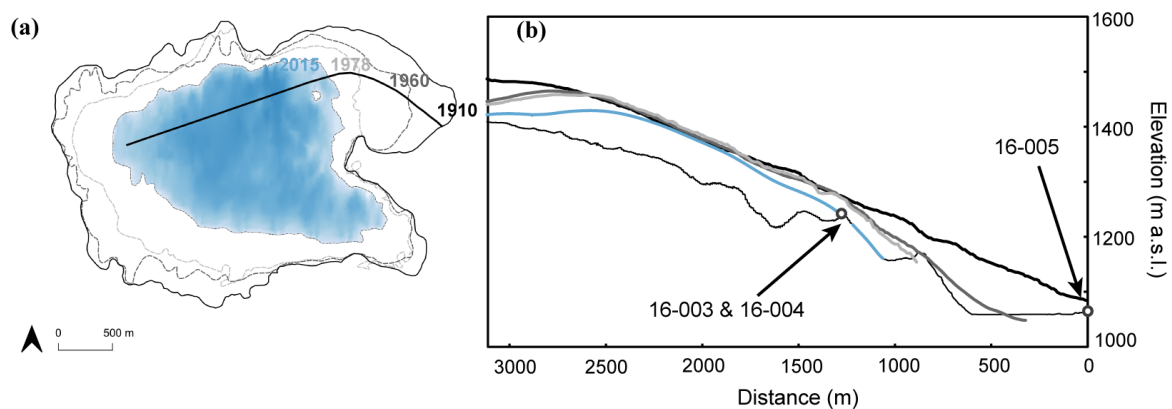


Figure S4: (a) Ice extents from 1910 to 2015 showing the ice reconstruction from 2015 (Fig. S3). (b) Ice profile reconstructions along the 1910 flow line in (a).



Figure S5: Prominent striations evident on bedrock knob emerging from Riukojietna northeast outlet glacier, in the vicinity of sample Riuko-16-003. Chisel for scale.

References

- Balco, G.: Production rate calculations for cosmic-ray-muon-produced ^{10}Be and ^{26}Al benchmarked against geological calibration data, *Quat. Geochronol.*, 39, 150–173, [doi:10.1016/j.quageo.2017.02.001](https://doi.org/10.1016/j.quageo.2017.02.001), 2017.
- Blaauw, M. and Christen, J. A.: Flexible paleoclimate age-depth models using an autoregressive gamma process, *Bayesian Analysis*, 6, 457–474, [doi:10.1214/11-BA618](https://doi.org/10.1214/11-BA618), 2011.
- Hallet, B., Hunter, L., Bogen, J.: Rates of erosion and sediment evacuation by glaciers: A review of field data and their implications, *Glob. Planet. Change*, 12, 213–235, [doi:10.1016/0921-8181\(95\)00021-6](https://doi.org/10.1016/0921-8181(95)00021-6), 1996.
- Heisinger, B., Lal, D., Jull, A. J. T., Kubik, P., Ivy-Ochs, S., Knie, K., and Nolte, E.: Production of selected cosmogenic radionuclides by muons: 2. Capture of negative muons, *Planet. Sc. Lett.*, 200, 357–369, [doi:10.1016/S0012-821X\(02\)00641-6](https://doi.org/10.1016/S0012-821X(02)00641-6), 2002a.
- Heisinger, B., Lal, D., Jull, A. J. T., Kubik, P., Ivy-Ochs, S., Neumaier, S., Knie, K., Lazarev, V., and Nolte, E.: Production of selected cosmogenic radionuclides by muons 1. Fast muons. *Planet. Sc. Lett.*, 200, 345–355, [doi:10.1016/S0012-821X\(02\)00640-4](https://doi.org/10.1016/S0012-821X(02)00640-4), 2002b.
- Knudsen, M. F., Egholm, D. L., and Jansen, J. D.: Time-integrating cosmogenic nuclide inventories under the influence of variable erosion, exposure, and sediment mixing, *Quat. Geochronol.*, 51, 110–119, [doi:10.1016/j.quageo.2019.02.005](https://doi.org/10.1016/j.quageo.2019.02.005), 2019.
- Lifton, N.: Implications of two Holocene time-dependent geomagnetic models for cosmogenic nuclide production rate scaling. *Planet. Sc. Lett.*, 433, 257–268, [doi:10.1016/j.epsl.2015.11.006](https://doi.org/10.1016/j.epsl.2015.11.006), 2016.
- Lifton, N., Sato, T. and Dunai, T. J.: Scaling *in situ* cosmogenic nuclide production rates using analytical approximations to atmospheric cosmic-ray fluxes, *Earth Planet. Sc. Lett.*, 386, 149–160, [doi:10.1016/j.epsl.2013.10.052](https://doi.org/10.1016/j.epsl.2013.10.052), 2014.
- Marrero, S. M., Phillips, F. M., Borchers, B., Lifton, N., Aumer, R., and Balco, G.: Cosmogenic nuclide systematics and the CRONUScal program, *Quat. Geochronol.*, 31, 160–187, [doi:10.1016/j.quageo.2015.09.005](https://doi.org/10.1016/j.quageo.2015.09.005), 2016.
- Phillips, F. M., Argento, D. C., Balco, G., Caffee, M. W., Clem, J., Dunai, T. J., Finkel, R., Goehring, B., Gosse, J. C., Hudson, A. M., Jull, A. J. T., Kelly, M. A., Kurz, M., Lal, D., Lifton, N., Marrero, S. M., Nishiizumi, K., Reedy, R. C., Schaefer, J., Stone, J. O. H., Swanson, T., and Zreda, M. G.: The CRONUS-Earth Project: A synthesis, *Quat. Geochronol.*, 31, 119–154, [doi:10.1016/j.quageo.2015.09.006](https://doi.org/10.1016/j.quageo.2015.09.006), 2016.
- Ploeg, K. and Stroeven, A. P.: History and dynamics of Fennoscandian Ice Sheet retreat, contemporary ice-dammed lake evolution, and faulting in the Torneträsk area, northwestern Sweden, *The Cryosphere*, 19, 347–373, [doi:10.5194/tc-19-347-2025](https://doi.org/10.5194/tc-19-347-2025), 2025.
- Stroeven, A. P., Hättestrand, C., Kleman, J., Heyman, J., Fabel, D., Fredin, O., Goodfellow, B. W., Harbor, J. M., Jansen, J. D., Olsen, L., Caffee, M. W., Fink, D., Lundqvist, J., Rosqvist, G. C., Strömberg, B., and Jansson, K. N.: Deglaciation of Fennoscandia, *Quaternary Sci. Rev.*, 147, 91–121, [doi:10.1016/j.quascirev.2015.09.016](https://doi.org/10.1016/j.quascirev.2015.09.016), 2016.